Unraveling Multicomponent Images by Extended Cross Correlation Analysis†

Bailin Zhang,‡ Shannon Yan, and Kopin Liu*

Institute of Atomic and Molecular Sciences (IAMS), Academia Sinica, P.O. Box 23-166 Taipei, Taiwan 10617

Received: April 13, 2007; In Final Form: May 24, 2007

In the course of studying the reaction dynamics of $F + CH_2D_2 \rightarrow HF + CHD_2$, several small features in the (2+1) REMPI spectra of the CHD_2 product were observed. Using the technique of imaging spectroscopy, those new features were identified and assigned to the 2_1^1, 3_1^1, and 5_1^1 bands. The ion velocity-mapped images acquired for those features, however, displayed severe overlaps with each other, rendering data analysis difficult. The extended cross correlation method was then applied for the first time in analyzing the ion images and successfully extracted the genuine pattern of each entangled component, which in turn enables us to focus on the dynamics information embedded in the multicomponent images.

I. Introduction

It has been amply demonstrated in a series of reports that the time-sliced ion velocity-imaging technique is a powerful method to reveal the product pair correlation in bimolecular scatterings.[1−12] The identification of the correspondence between the state-pair and the observed image feature rests on the conservations of energy and momentum, provided that all energetics are known.[12] Otherwise, one can go in the opposite direction by using the image feature to identify the unknown product state or to assign a previously unidentified REMPI (resonance-enhanced multiphoton ionization) spectral peak, as demonstrated recently for the 1_1^1, 3_1^1, and 4_1^1 bands of the CD_3 radical.[13] We dubbed this approach imaging spectroscopy or spectroscopy by imaging. In the first part of this paper we apply imaging spectroscopy to the CHD_2 radical, identifying two previously unobserved REMPI transitions, 2_1^1 and 5_1^1, in addition to the 0_0^0, 1_1^1, and 3_1^1 bands, from the reaction $F + CH_2D_2 \rightarrow CHD_2 + HF$.

When the probe laser frequency was held fixed at these bands, however, the acquired images display contaminations from the spectrally adjacent bands, resulting in severe overlaps of several components on image features. Observing an overlapped image has been noted in the past. If the energetics is such that the contributions from different components or sources can be resolved from the target one in the product recoil speed distribution P(U), then a simple subtraction scheme suffices to pull out the desired speed distribution—provided that the speed distribution of the contaminant is known from an independent, single-component image. This is the case found previously for the $CHD_2(3_1^1)$ image from $F + CHD_3 \rightarrow CHD_2 + DF$.[14] More recently we encountered another type of overlapping images. To explore mode-specific reaction dynamics in $Cl + CHD_3$ using pair-correlation measurements, a tunable IR (infrared) laser was used to excite the CHD_3 reagent to $\upsilon_1 = 1$, i.e., one-quantum excitation of the C−H bond. The IR-on image of the $CD_3(\upsilon=0)$ product clearly exhibits features from both the stretch-excited and the unpumped ground-state reactants. Since the two product channels of $Cl + CHD_3(\upsilon_1=1) \rightarrow HCl(\upsilon'=1) + CD_3(\upsilon=0)$ and $Cl + CHD_3(\upsilon=0) \rightarrow HCl(\upsilon'=0) + CD_3(\upsilon=0)$ are nearly degenerate, a complete overlap of their respective features on the image was observed. A threshold method was then developed to determine the fraction of vibrationally excited CHD_3 in the molecular beam, with which the mode-specific dynamics from the stretched-excited reaction can then be uncovered.[15]

As will be shown here, the overlapped images in the present paper are of a different nature. We resorted to a more elaborate method, extended cross correlation (XCC),[16,17] to unravel the overlapped interferences and to recover dynamics information from the multicomponent images. The XCC method is one of many data analysis techniques to identify and extract multiple patterns from experimental data. It is a pattern recognition-based rather than a model-based method. Like several other similar techniques, such as covariance mapping[18] and principal component analysis,[19,20] it assumes that a set of spectra can be regarded as linear combinations of patterns. The coefficients of the patterns represent their contributions to a given spectrum. As long as those patterns are not completely overlapped, the ratios of their coefficients can be drawn out from the recursion map in the XCC technique, with which the desired pattern for each individual component can then be recovered. The interested readers are referred to refs 16 and 17 for the basic concept of XCC and the merits compared to other similar data analysis methods.

II. Experimental Section

The crossed-beam apparatus and experimental details have been presented previously.[21,22] Only a brief description of relevant points will be given here. A discharged, pulsed beam of a mixture of 5% F_2 in Ne was used to generate the F-atom,[22,23] and the supersonic expansion of neat CH_2D_2 yielded the target beam. Two pulsed beams cross in a differentially pumped scattering chamber. The reaction product CHD_2 was interrogated by a (2+1) REMPI scheme via its $3p^2\,B_1 \leftarrow \tilde{X}^2\,B_1$ transition.[14,24] The UV probe laser, near 333 nm, was about 8−10 mJ pulse^{-1} and was softly focused through a $f = 50$ cm cylindrical lens. A time-sliced velocity imaging technique then mapped the recoils of the state-tagged CHD_2^+ ion.[21]

† Part of the "Sheng Hsien Lin Festschrift".

* Corresponding author e-mail: kpliu@gate.sinica.edu.tw.

‡ Present address: Department of Chemistry, Wayne State University, Detroit, MI 48202.

10.1021/jp072916z CCC: $37.00
Published on Web 07/17/2007

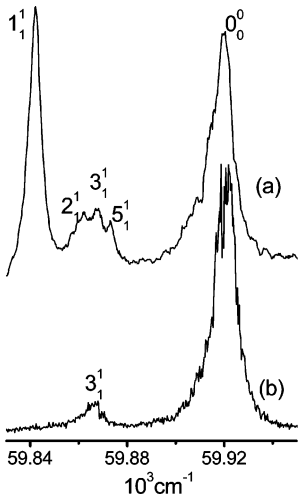

Figure 1. Examples of two REMPI spectra of the CHD_2 radical products near the origin band from (a) the reaction $F + CH_2D_2 \rightarrow CHD_2 + HF$ at $E_c = 0.42$ kcal/mol and (b) the reaction $F + CHD_3 \rightarrow CHD_2 + DF$ at $E_c = 2.76$ kcal/mol.

TABLE 1: Vibrational Frequencies and the Spectral Shifts, All in cm^{-1}, in the (2+1) REMPI Detection of the CHD_2 Radical [f]

state	$\upsilon_1(a_1)$	$\upsilon_2(a_1)$	$\upsilon_3(a_1)$	$\upsilon_4(b_1)$	$\upsilon_5(b_2)$	$\upsilon_6(b_2)$
X^2B_1	3116[a]	2221[a]	1034[a]	510[b]	2413[e]	(1248)[c]
shift from 0_0^0	−79	−60	−53	655	−48	
$3p^2B_1$	3037[e]	2161[e]	981[d]	1165	2365[b]	1210[b]

[a] Reference 25. [b] Reference 24. [c] Reference 26. [d] Reference 14. [e] This work, deduced from the spectral shift from the 0_0^0 band. The frequencies of the υ_1 and υ_2 modes in the $3p^2B_1$ state agree with ref 24 within a few cm^{-1}. [f] The origin band 0_0^0 is at 59 921 cm^{-1}.

III. Results and Discussion

(A) Identification of the REMPI Bands. Figure 1 exemplifies the REMPI spectra, around the origin band 0_0^0, of the CHD_2 radical from two different reactions, $F + CH_2D_2 \rightarrow CHD_2 + HF$ at $E_c = 0.42$ kcal/mol and $F + CHD_3 \rightarrow CHD_2 + DF$ at $E_c = 2.76$ kcal/mol, respectively. In the case of $F + CHD_3$, in addition to the prominent 0_0^0 band, a small feature was seen, which was ascribed previously to the CHD_2 3_1^1 band.[14] The REMPI spectrum for the reaction $F + CH_2D_2$, however, indicates richer product state distributions. Besides 0_0^0 and 3_1^1 bands, a strong peak labeled as 1_1^1 (vide infra) and two weaker (adjacent to the 3_1^1 peak) features labeled as 2_1^1 and 5_1^1 (vide infra) were seen.

The assignments of those bands are based on the following. As summarized in Table 1, from the resonance Raman spectrum of CHD_2, Westre et al. obtained υ_1 (the CH stretching fundamental) = 3116.2 cm^{-1}, υ_2 (the CD_2 symmetric stretch) = 2221.5 cm^{-1}, and υ_3 (the CD_2 scissors) = 1034.2 cm^{-1} for the electronic ground state $\tilde{X}^2B_1$.[25] Using (2+1) REMPI spectroscopy Brum et al. reported υ_4 (the out-of-plane bend) = 510 cm^{-1} for $\tilde{X}^2B_1$ as well as the fundamental frequencies of five modes (except υ_3) in the excited $3p^2B_1$ state.[24] Given the above and from the observed spectral shifts of those new features from the 0_0^0 band, the 1_1^1 and 2_1^1 transitions were then assigned. To our best knowledge, no previous experiment reported the υ_5 (the CD_2 antisymmetric stretch) and the υ_6 (the CH bend) modes of the $\tilde{X}^2B_1$ state; theoretically, a high level ab initio calculation predicted 2358 and 1248 cm^{-1} for υ_5 and υ_6, respectively.[26] To identify the nature of the remaining feature that is blue-shifted from 3_1^1 or red-shifted 48 cm^{-1} from the 0_0^0 peak, we resorted to the imaging spectroscopy method.

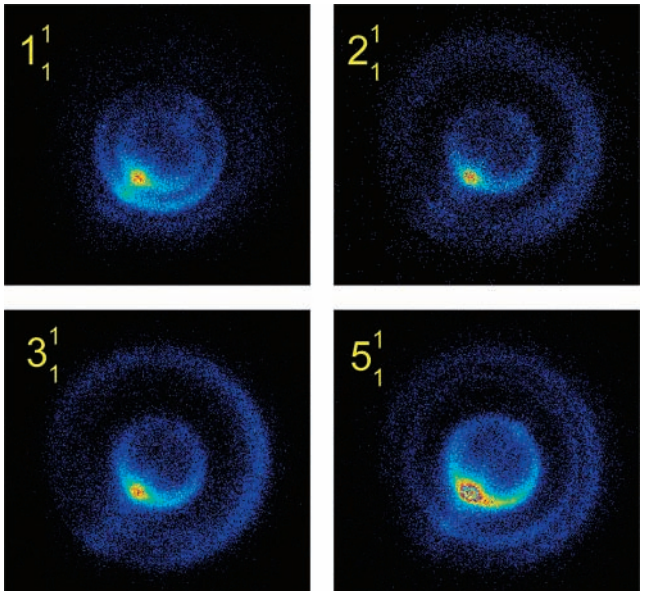

Figure 2. Four raw images of the CHD_2 products from the $F + CH_2D_2$ reaction at $E_c = 2.32$ kcal/mol. The probe laser frequencies were fixed at the peaks of the four respective bands, labeled in Figure 1(a).

In that approach the image of the reaction products CHD_2 was acquired with the probe laser wavelength fixed at the (unassigned) spectral peak. The exothermicity of the reaction $F + CH_2D_2 \rightarrow HF + CHD_2$ is known, $\Delta H_0^0 = -31.63$ kcal/mol.[1,25,26] By conservation of energy, the possible state-pair of the two reaction products was then sought to match the resolved ringlike structures on the image. Figure 2 presents four raw images of CHD_2 from the $F + CH_2D_2$ reaction at $E_c = 2.32$ kcal/mol with the probe laser frequencies parked at the peaks of the four respective bands. The 1_1^1 image is characterized by an intense double-ring structure, which is significantly different from the other three images. While the general patterns of the latter three are similar, subtle differences in the widths and the splitting of the outer rings are noticeable.

The similarity and the difference of these images are better appreciated in the P(U) distributions, for which the density-to-flux corrections have been made.[21,27] The results are presented in Figure 3, in which the anticipated energetic limits of the product state-pairs were calculated and shown as the vertical dotted lines. From the relative intensities of the features in P(U) distributions, the above assignments of the 1_1^1, 2_1^1, and 3_1^1 bands are confirmed. Since the vibrational frequencies of the υ_5 and υ_6 modes in the upper $3p^2B_1$ state are known (Table 1), the corresponding frequencies in the $\tilde{X}^2B_1$ state can be obtained from the spectral shift of −48 cm^{-1} (from the 0_0^0 peak) for the unknown, up to this point, feature (labeled as 5_1^1 in Figure 1). Thanks to the large difference in the vibrational frequencies of υ_5 and υ_6 modes, the distinct structure at $\mu_{CHD_2} \sim 1.1$ km/s in the right lower panel of Figure 3 then provides the evidence in support of the present assignment of the 5_1^1 band. This completes the REMPI assignments shown in Figure 1.

(B) Removing the Contributions of $v = 0$ and $v_1 = 1$ from Images. As can be clearly seen from Figure 3, none of those four images can be ascribed as straightforward state-pairs from the labeled REMPI-bands, due to the spectral congestion. Worse yet, their product recoil speed distributions P(U) are complicated by heavily overlapped structures from several different components. To unravel the reaction dynamics from those multi-

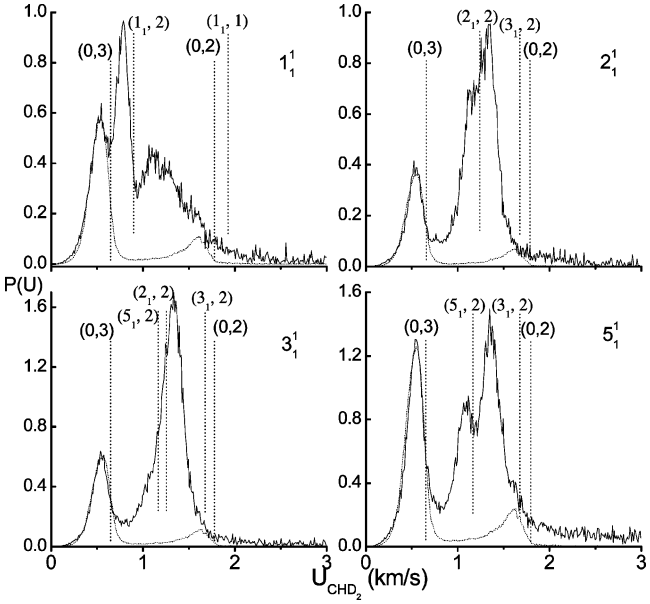

Figure 3. The derived CHD_2 product speed distributions P(U), in the center-of-mass frame, from the four images shown in Figure 2. The vertical dotted lines give the energetic-allowed speeds of the indicated product state pairs (v_{CHD_2}, v_{HF}). The dotted curve in the four panels illustrates the contribution from the spectral tail of the 0_0^0-band, which is taken from Figure 4.

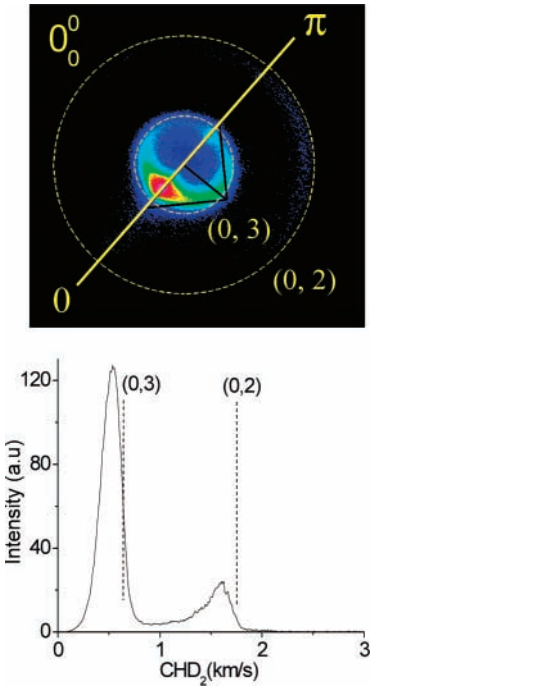

Figure 4. The raw image of the CHD_2 product probed by fixing the probe laser frequency at the peak of the 0_0^0 origin band. Shown in the lower portion is the resultant product speed distribution with the assigned state-pairs as indicated.

component images, a two-step procedure was adapted. First, we will subtract the features associated with the CHD_2(v=0 and v_1=1) states from those images in this subsection. Then in the next subsection we will introduce a more elaborate algorithm to extract the correlated information for the v_2, v_3, and $v_5 = 1$ products.

Figure 4(a) shows the raw image when the λ_{probe} was fixed at the peak of 0_0^0 band, and Figure 4(b) depicts the corresponding P(U) distribution at $E_c = 2.32$ kcal/mol. Clearly, this product image is dominated by the state-pairs of (0_0, 3) and (0_0, 2) without any trace of contaminations from the adjacent spectral features. [Herein, we denote the state-pair as (v_{CHD_2}, v_{HF}).] Its P(U) distribution is also displayed as the dotted curve in all four panels of Figure 3 by matching the slowest (0, 3) structures, respectively. A closer inspection of the four resultant P(U) distributions, with the (v=0)-contribution removed, indicates that the one for 1_1^1 is distinctly different from the other three. We ascribed it to a distribution mainly from the (1_1, 2) and (1_1, 1) pairs, i.e., the "pure" 1_1-P(U) distribution, though possible small contributions from the (2_1, 2), (3_1, 2), and (5_1, 2) product pairs cannot be ruled out.

Exemplified in Figure 5(a) is the resultant P(U) distribution for 3_1^1 without the CHD_2(v=0) contribution. Also shown as the dotted curve (labeled 1_1) is the contribution from the "pure" 1_1-distribution as just described. Note the minor 1_1-contribution to the 3_1^1 distribution. Hence, even if the 1_1-distribution is not as pure as we have claimed, it has little consequence on the results to be presented. Subtracting it from the 3_1^1 distribution then yields a new 3_1^1 without the contaminations from both the 0_0 and 1_1 components, as shown in Figure 5(c). Similar analyses were then performed for the 2_1^1 and 5_1^1 distributions in Figure 3, and the results are shown in Figure 5 (parts (b) and (d), respectively).

(C) Extended Cross-Correlation Analysis of the 2_1^1, 3_1^1, and 5_1^1 Distributions. Using the successive, simple subtraction scheme, we obtained the distributions for 2_1^1, 3_1^1, and 5_1^1 (Figure

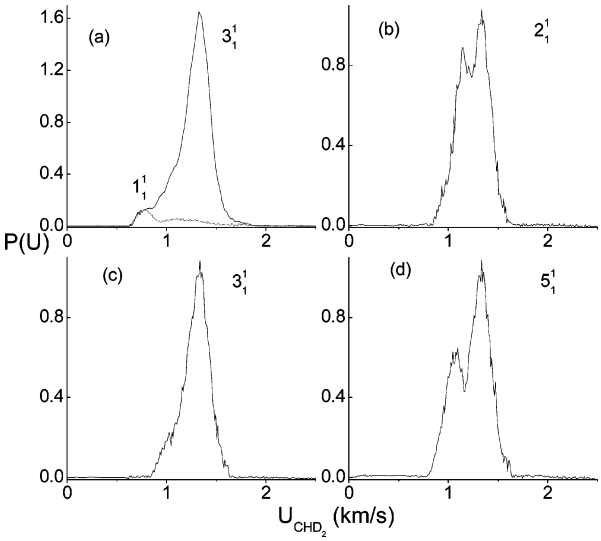

Figure 5. Illustrated in (a) is the speed distribution for the "reduced" 3_1^1-P(U) from Figure 3, for which the contribution from 0_0^0 has been removed. The dotted curve, labeled 1_1, represents the contribution from the spectral contamination of the 1_1^1-band, which is obtained by subtracting the 0_0^0-contribution from the 1_1^1-distribution shown in the top panel of Figure 3. Shown in (c) is the resultant distribution after the 1_1-contamination being removed from 3_1^1 as illustrated in (a). Similarly, (b) and (d) yield the distributions for 2_1^1 and 5_1^1, respectively, which are free of the contributions from 0_0^0 and 1_1^1.

5(b)−(d)) that are free from the contaminations from the 0_0 and 1_1 states. The three resultant distributions are, however, similar and display heavily overlapped structures. To disentangle the multicomponent distributions unambiguously and in a more robust manner, we have to call upon more elaborate pattern recognition methods. Specifically, XCC (extended cross correlation) was applied to recover information from the entangled distributions shown in Figure 5(b)−(d).

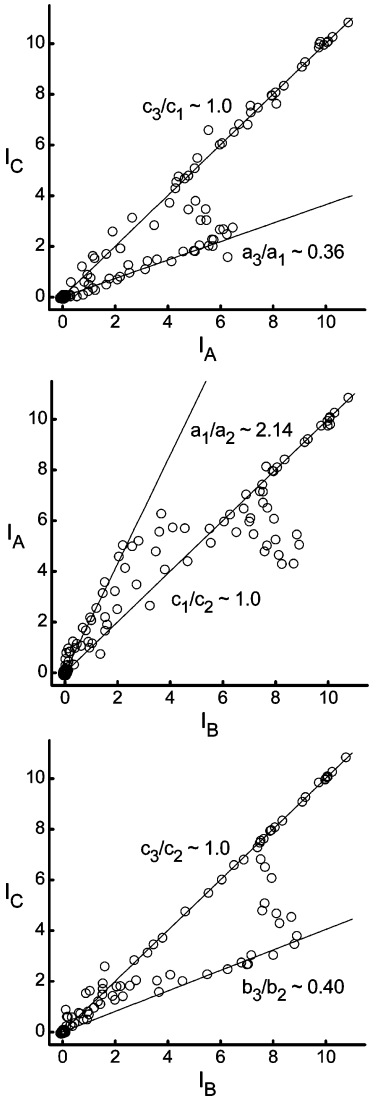

Figure 6. Three recursion maps with each point on the map representing the intensities in the two P(U) distributions at the same speed. The ratio directions (or the slopes) for all three c_i's are unity, validating the use of eq 4.

XCC is one of many data analysis methods. It is a pattern recognition-based technique designed to identify and recover patterns that are interfered or overlapped in multicomponent spectra; and it can be applied in a model-free manner. We adapted it here because of its straightforward application, and more importantly that this approach does not require the experimental intensity normalization of the images or distributions involved.

To apply XCC to the present problem, we first assume that the three P(U) distributions shown in Figure 5(b)−(d) are the result of linear combinations of three genuine patterns for the 2_1, 3_1, and 5_1 states.

That is,

$$\text{for } \lambda \text{ at } 5_1^1: \; I_A = a_1 I_{5_1} + b_1 I_{2_1} + c_1 I_{3_1} \tag{1}$$

$$\text{for } \lambda \text{ at } 2_1^1: \; I_B = a_2 I_{5_1} + b_2 I_{2_1} + c_2 I_{3_1} \tag{2}$$

$$\text{for } \lambda \text{ at } 3_1^1: \; I_C = a_3 I_{5_1} + b_3 I_{2_1} + c_3 I_{3_1} \tag{3}$$

Here, the I_A, I_B, and I_C represent the distributions in Figure 5(b)−(d), and I_{5_1}, etc. denote the true patterns or distributions of the product states (e.g., v_5=1) from the reaction. The coefficients a_i, b_i, and c_i describe the relative weights of the patterns in each observed P(U) distribution shown in Figure 5(b)−(d). The goal is then to determine those coefficients in a least-biased and model-free way, which can be achieved in XCC by the so-called recursion map.[16,17] Although a three-dimensional recursion map has been generated from eqs 1−3, it turned out to be problematic for the present case, presumably because one of the components is almost completely overlapped with the other two (vide infra). We adopted instead a two-dimensional approach, operated in a sequential manner, to provide an intuitive understanding of the underlying concept of the XCC method.

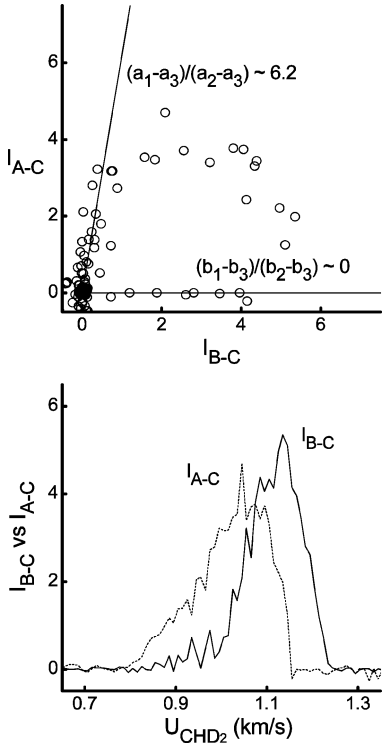

Figure 7. The lower portion shows the two speed distributions with the I_{3_1}-component removed, I_{A-C} and I_{B-C}. Their recursion map is displayed in the upper portion. The slope $(b_1-b_3)/(b_2-b_3) = 0$ gives $b_1 = b_3$, implying that I_A and I_C contain about the same amounts of I_{2_1}.

Once again, the advantage of using the XCC approach is that there is no need to experimentally normalize the entangled distributions. Hence, we are free to scale the I_A, I_B, and I_C distributions (Figure 5(b)−(d)) to the same peak heights. Energetically, those dominant peaks are almost entirely attributed to the I_{3_1} components, thus we have $c_1 \approx c_2 \approx c_3 \approx 1$, as will be demonstrated shortly. Equations 1−3 can be, for the time being, rewritten in a shorthand matrix form

	I_{5_1}	I_{2_1}	I_{3_1}
I_A	a_1	b_1	1
I_B	a_2	b_2	1
I_C	a_3	b_3	1

(4)

We first examined the recursion maps among them, as shown in Figure 6. What is plotted here are the intensity values

in either of two distributions. That is, the coordinates of each point represent the intensities in the two distributions at a given speed of CHD_2 products. Also shown are the straight lines passing through the origin. The points that cluster around the straight line have signal content that can be in general associated with one of the genuine patterns. In other words, these points correspond to the CHD_2 speeds at which nonoverlapped features are found in the two distributions; hence, the slopes of these lines give the ratios of the corresponding coefficients. As is seen, the ratios of all three c_i coefficients are indeed unity, justifying eq 4. However, what remains are only three other slopes or ratios that are not sufficient to obtain the six unknowns in (4).

Taking advantage of $c_1 = c_2 = c_3 = 1$, we examined next the distributions without the I_{3_1} contributions, i.e.

	I_{5_1}	I_{2_1}
I_{A-C}	a_1-a_3	b_1-b_3
I_{B-C}	a_2-a_3	b_2-b_3

(5)

The resultant difference distributions are displayed in Figure 7, along with their recursion map. A slope of zero for $(b_1\text{-}b_3)/(b_2\text{-}b_3)$ suggests that $b_1 = b_3$ or that I_A and I_C contain about the same amounts of I_{2_1}, which further implies that the I_{A-C} distribution closely resembles the genuine I_{5_1} pattern, which is proportional to $(a_1\text{-}a_3)I_{5_1}$. Given that and the two slopes a_1/a_2, a_3/a_1 shown in Figure 6, all three amplitudes $a_1I_{5_1}$, $a_2I_{5_1}$, and $a_3I_{5_1}$ can then be obtained with the coefficients $a_1 = 1.572$, $a_2 = 0.733$, and $a_3 = 0.572$.

From the above, eq 4 is now reduced to eq 6, i.e., only two

	I_{5_1}	I_{2_1}	I_{3_1}
I_A	1.572	b_3	1
I_B	0.733	b_2	1
I_C	0.572	b_3	1

(6)

unknowns remain. It is worth mentioning that the slope $(a_1\text{-}a_3)/(a_2\text{-}a_3) = 6.2$, which is entirely consistent with the values of a_1/a_2 and a_3/a_1 shown in Figure 6, also indicates that the amount of I_{5_1} in I_{B-C} is about 0.16 (or 1/6.2) of that in I_{A-C}, which is pure I_{5_1}. Thus, $I_{B-C} = 0.16I_{5_1} + (b_2\text{-}b_3)I_{2_1}$. Knowing I_{5_1} and the ratio of b_3/b_2 from Figure 6, one could then deduce the profiles of $b_2I_{2_1}$ and $b_3I_{2_1}$ from I_{B-C} (Figure 7) based on the above equation for I_{B-C}, yielding $b_2 = 1.677$ and $b_3 = 0.677$. Once this is done, the profile of I_{3_1} can then be deduced from each I_A, I_B, and I_C. The resultant I_{3_1}'s, unfortunately, all showed significant negative-going signals around the peak of I_{2_1} distribution—a physically unreasonable result.

To trace the source of this error, we took an alternative approach. Since I_{5_1} is known as I_{A-C} from eq 6, presented in Figure 8 are the two distributions of I_{B-5_1} and I_{C-5_1}, which are without the contributions from I_{5_1}. Their difference must then be entirely due to $(b_2\text{-}b_3)I_{2_1}$, and their recursion map yields a value of $b_3/b_2 = 0.158$, which is in significant variance with the above value of 0.40 given from Figure 6. (We will comment on this discrepancy later.) Using this alternative ratio to extract the amplitudes of I_{2_1} in each I_A, I_B, and I_C, we obtained $b_2 =$

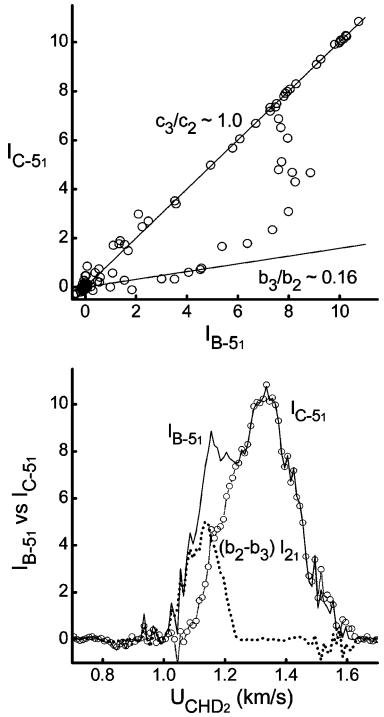

Figure 8. An alternative way for applying the XCC analysis. Presented in the lower panel are the two speed distributions with the 5_1-component removed, I_{B-5_1} and I_{C-5_1}, and in the upper part is their recursion map.

1.187 and $b_1 = b_3 = 0.187$. And the I_{3_1}'s thus derived appeared to be self-consistent and physically more reasonable. Figure 9 presents the decomposition of the three entangled I_B, I_A, and I_C distributions. And the final matrix becomes

	I_{5_1}	I_{2_1}	I_{3_1}
I_A	1.572	0.187	1
I_B	0.733	1.187	1
I_C	0.572	0.187	1

(7)

The small negative values (near the peak of I_{5_1}) for I_{3_1} suggest a slight error in I_{5_1}, presumably arising from the slope uncertainty of the recursion map shown in Figure 7. It also becomes clear from Figure 9 that the I_{2_1} components are entirely overlapped with either I_{3_1} over the high-speed end or I_{5_1} over the slower end. And the amplitudes of I_{2_1} in either I_A or I_C are much smaller than the other two components. As a result, the intensities of I_C (thus also I_A) in this particular speed range are severely contaminated, yielding a "biased" b_3/b_2 ratio in the primitive recursion map between I_C and I_B (Figure 6).

As is readily seen, the retrieved speed distributions for the $(3_1, 2)$, $(2_1, 2)$, and $(5_1, 2)$ product pairs display peaks that deviate somewhat from the calculated, respective energetic limits. The degrees of deviation represent the rotational energy excitations of the two product pairs. Simple analysis, by virtue of energy conservation, reveals that the average rotational energy contents for $(5_1, 2)$, $(2_1, 2)$, and $(3_1, 2)$ are about 0.64, 1.1, and 2.6 kcal/mol, respectively. In other words, the correlated rotational excitation of the HF(v=2) product is significantly higher when the CHD_2 coproduct is formed with one quantum excitation in the CD_2 scissors mode (v_3) than in the CD_2

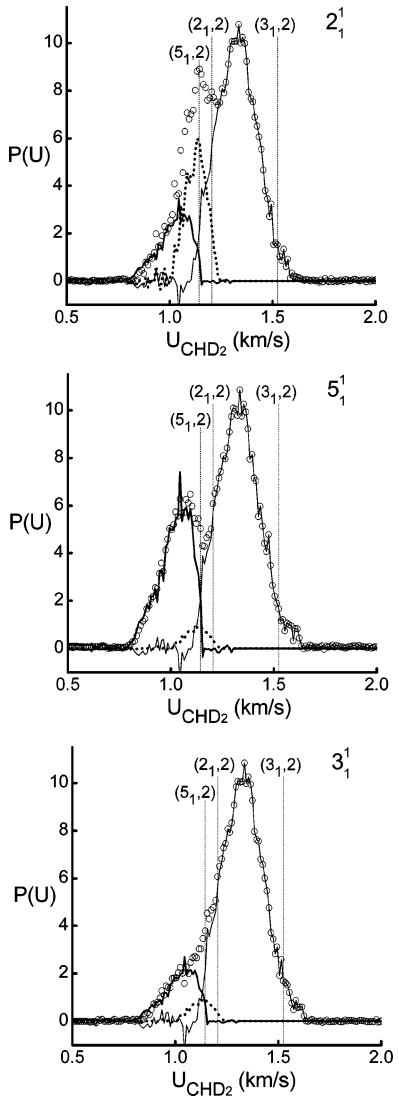

Figure 9. Final results, showing the partitions of the three heavily overlapped 2_1^1, 5_1^1, and 3_1^1 distributions. A closer comparison of the resultant 3_1-component, obtained from each of the three distributions, reveals that they are nearly superimposable, indicating the self-consistency of the present XCC analysis.

symmetric (υ_2) or asymmetric (υ_5) stretch. The implication of this finding to reaction dynamics will be discussed in a future report on this reaction over a wide range of initial collision energies.

IV. Summary

Two contributions are reported in this work. First, using the imaging spectroscopy technique,[13,14] two new REMPI bands, 2_1^1 and 5_1^1, of the CHD_2 radical are identified from the reaction $F + CH_2D_2 \rightarrow HF + CHD_2$. Both bands are heavily overlapped with the 3_1^1 transition and to a lesser extent with the 0_0^0 and 1_1^1 features. The ion velocity-mapped images of the 3_1^1, 2_1^1, and 5_1^1 bands show severe interferences from each other and from the tails of the more intense 0_0^0 and 1_1^1 bands. Using the simple subtraction scheme, the contributions from the latter two can be removed easily. Extended cross correlation analysis[16,17] was then exploited to unravel the interferences and to recover the genuine speed distribution of each individual component. With the methodology established, a copious set of image data over a wide range of collisional energies can then be analyzed to reveal the pair-correlated reaction dynamics, which will be reported in the near future.

Acknowledgment. We are indebted to Y.-T. Wu and H.-Y. Liao for their help in acquiring some of the data of this project. This work was supported by the National Science Council of Taiwan under NSC 95-2119-M-001-002.

References and Notes

(1) Lin, J. J.; Zhou, J.; Shiu, W.; Liu, K. *Science* **2003**, *300*, 966.
(2) Zhou, J.; Lin, J. J.; Shiu, W.; Liu, K. *J. Chem. Phys*. **2003**, *119*, 4997; *Phys. Chem. Chem. Phys*. **2006**, *8*, 3000.
(3) Shiu, W.; Lin, J. J.; Liu, K.; Wu, M.; Parker, D. H. *J. Chem. Phys*. **2004**, *120*, 117.
(4) Zhou, J.; Lin, J. J.; Liu, K. *J. Chem. Phys.* **2004**, *121*, 813.
(5) Shiu, W.; Lin, J. J.; Liu, K. *Phys. Rev. Lett*. **2004**, *92*, 103201.
(6) Zhou, J.; Shiu, W.; Lin, J. J.; Liu, K. *J. Chem. Phys*. **2004**, *120*, 5863; *J. Chem. Phys*. **2006**, *124*, 104309.
(7) Zhou, J.; Lin, J. J.; Zhang, B.; Liu, K. J. *Phys. Chem. A* **2004**, *108*, 7832.
(8) Zhou, J.; Zhang, B.; Lin, J. J.; Liu, K. *Mol. Phys*. **2005**, *103*, 1757.
(9) Zhang, B.; Liu, K. *J. Chem. Phys*. **2005**, *122*, 101102; *J. Phys. Chem. A* **2005**, *109*, 6791.
(10) Zhang, B.; Shiu, W.; Lin, J. J.; Liu, K. *J. Chem. Phys.* **2005**, *122*, 131102.
(11) Zhang, B.; Shiu, W.; Liu, K. *J. Phys. Chem. A* **2005**, *109*, 8983; *J. Phys. Chem. A* **2005**, *109*, 8989.
(12) Liu, K. *Phys. Chem. Chem. Phys.* **2007**, *9*, 17; *J. Chem. Phys.* **2006**, *125*, 132307.
(13) Zhang, B.; Zhang, J.; Liu, K. *J. Chem. Phys*. **2005**, *122*, 104310.
(14) Zhou, J.; Lin, J. J.; Liu, K. *J. Chem. Phys*. **2003**, *119*, 8289.
(15) Yan, S.; Wu, Y.-T.; Liu, K. *Phys. Chem. Chem. Phys*. **2007**, *9*, 250.
(16) Jacobson, M. P.; Coy, S. L.; Field, R. W. *J. Chem. Phys.* **1997**, *107*, 8349.
(17) Coy, S. L.; Jacobson, M. P.; Field, R. W. *J. Chem. Phys.* **1997**, *107*, 8357.
(18) Frasinski, L. J.; Codling, K.; Hatherly, P. A. *Science* **1989**, *246*, 973.
(19) Hercules, D. M.; Houalla, M.; Proctor, A.; Fiedor, J. N. *Anal. Chem. Acta* **1993**, *283*, 42.
(20) Fiedor, J. N.; Proctor, A.; Houalla, M.; Hercules, D. M. *Surf. Interface Anal*. **1993**, *20*, 1.
(21) Lin, J. J.; Zhou, J.; Shiu, W.; Liu, K. *Rev. Sci. Instrum.* **2003**, *74*, 2495; *Chin. J. Chem. Phys*. **2004**, *17*, 346.
(22) Zhou, J.; Lin. J. J.; Shiu, W.; Pu, S.-C.; Liu, K. *J. Chem. Phys*. **2003**, *119*, 2538.
(23) Dong, F.; Lee, S.-H.; Liu, K. *J. Chem. Phys*. **2000**, *113*, 3633.
(24) Brum, J. L.; Johnson, R. D., III; Hudgens, J. W. *J. Chem. Phys*. **1993**, *98*, 3732.
(25) Westre, S. G.; Liu, X.; Getty, J. D.; Kelly, P. B. *J. Chem. Phys*. **1991**, *95*, 8793.
(26) Mebel, A. M.; Lin, S.-H. *Chem. Phys*. **1997**, *215*, 329.
(27) Sonnenfroh, D. M.; Liu, K. *Chem. Phys. Lett*. **1991**, *176*, 183.